SiO2/Ladder-Like Polysilsesquioxanes Nanocomposite Coatings: Playing with the Hybrid Interface for Tuning Thermal Properties and Wettability

Terms of use:

(Article begins on next page)

25 April 2024

SiO2/Ladder-Like Polysilsesquioxanes Nanocomposite Coatings: Playing with the Hybrid Interface for Tuning Thermal Properties and Wettability

Massimiliano D'Arienzo [1,*], **Sandra Dirè** [2,3,*] , **Elkid Cobani** [1], **Sara Orsini** [1],
Barbara Di Credico [1] , **Carlo Antonini** [1] , **Emanuela Callone** [2,3], **Francesco Parrino** [2],
Sara Dalle Vacche [4,5] , **Giuseppe Trusiano** [4] , **Roberta Bongiovanni** [4,5] **and Roberto Scotti** [1]

1. Department of Materials Science, INSTM, University of Milano-Bicocca, Via R. Cozzi 55, 20125 Milano, Italy; e.cobani@campus.unimib.it (E.C.); s.orsini2@campus.unimib.it (S.O.); barbara.dicredico@unimib.it (B.D.C.); carlo.antonini@unimib.it (C.A.); roberto.scotti@unimib.it (R.S.)
2. Department Industrial Engineering, University of Trento, Via Sommarive 9, 38123 Trento, Italy; emanuela.callone@unitn.it (E.C.); francesco.parrino@unitn.it (F.P.)
3. "Klaus Müller" Magnetic Resonance Lab., Department of Industrial Engineering, University of Trento, Via Sommarive 9, 38123 Trento, Italy
4. Department of Applied Science and Technology, DISAT, Politecnico di Torino, Corso Duca degli Abruzzi 24, 10129 Torino, Italy; sara.dallevacche@polito.it (S.D.V.); giuseppe.trusiano@polito.it (G.T.); roberta.bongiovanni@polito.it (R.B.)
5. Consorzio Interuniversitario Nazionale per la Scienza e Tecnologia dei Materiali, (INSTM) Via G. Giusti, 9, 50121 Firenze, Italy
* Correspondence: massimiliano.darienzo@unimib.it (M.D.); sandra.dire@unitn.it (S.D.)

Abstract: The present study explores the exploitation of ladder-like polysilsesquioxanes (PSQs) bearing reactive functional groups in conjunction with SiO2 nanoparticles (NPs) to produce UV-curable nanocomposite coatings with increased hydrophobicity and good thermal resistance. In detail, a medium degree regular ladder-like structured poly (methacryloxypropyl) silsesquioxane (LPMASQ) and silica NPs, either naked or functionalized with a methacrylsilane (SiO2@TMMS), were blended and then irradiated in the form of a film. Material characterization evidenced significant modifications of the structural organization of the LPMASQ backbone and, in particular, a rearrangement of the silsesquioxane chains at the interface upon introduction of the functionalized silica NPs. This leads to remarkable thermal resistance and enhanced hydrophobic features in the final nanocomposite. The results suggest that the adopted strategy, in comparison with mostly difficult and expensive surface modification and structuring protocols, may provide tailored functional properties without modifying the surface roughness or the functionalities of silsesquioxanes, but simply tuning their interactions at the hybrid interface with silica fillers.

Keywords: nanocomposites; silsesquioxanes; hybrid materials; interfaces; hydrophobic properties; coating

1. Introduction

The increasing demand of electronic devices has stimulated significant efforts to enhance their stability and lifespans [1–3]. In fact, a degradation of the electrical performance over the use period can be clearly observed, whose main origin lies in water permeation under ambient conditions [1,4].

A possible solution to face this issue is, in the design and development of any device, the application of coating materials with improved water repellence [5–8].

Polymer nanocomposites have received increasing attention when a defined adjustment of the coating wettability is required [5,7–10]. The hydrophobicity can be tailored mostly by (i) controlling roughness at the microscale and (ii) functionalizing the surface of nanocomposites with low-surface energy materials with long alkyl chains or fluorinated functional groups [11–13].

In this context, fluorocarbon polymers (e.g., polytetrafluoroethylene—PTFE) have been utilized for the generation of hydrophobic surfaces, owing to their remarkably low surface energies [14]. Silane compounds, particularly organoalkoxysilanes and fluorinated organosilanes, have also been widely used as building blocks to develop hybrid materials with high water repellence [15–19]. However, fluorinated, especially fluoroalkyl, compounds display several economic and ecological drawbacks, namely their high cost and potential risk to human health and the environment in the case of skin contact and fluorine emission from the coating application, which is usually performed at high temperature [20]. This was also witnessed in the efforts of the European Community in the restriction of per- and polyfluoroalkyl substance (PFAS) use [21]. Therefore, the production of non-fluorinated hydrophobic coatings applicable at relatively low temperature represents a key task, even more so in terms of their ecofriendly use.

Several methods are followed to tune the surface roughness and thus the hydrophobicity/hydrophilicity of a coating: mechanical stretching, physical etching (laser, plasma), chemical etching, lithography, sol–gel processing, electrochemical reactions, or chemical deposition by CVD [22,23]. Recently, nanoparticles (NPs) have been exploited to produce tailored surface roughness at the sub-micrometer scale. The approach consists of the deposition of pre-formed NPs to a fine surface or microroughness or their dispersion in a polymer solution and subsequent spraying onto a smooth surface [24,25]. The possibility of precisely controlling particle size and shape makes this method particularly powerful in the wettability engineering of a surface [26]. Nevertheless, the NPs' aggregation onto a fabricated rough surface leads to poor mechanical durability, hampering the practical application of the coatings [27].

Polysilsesquioxanes (PSQs), a class of emerging hybrid materials derived from trifunctional silanes, appear promising candidates to face the above issues [8,28–31]. These inorganic polymeric materials can provide both remarkable thermomechanical properties and water repellency, owing to the presence of tunable peripheral organic groups, which may also offer compatibility, dispersion stability, and reactivity [28–31]. PSQs can be classified into either random or random branched structures [32], polyhedral oligomeric silsesquioxanes (POSS) [33–38], and fully condensed ladder-like polysilsesquioxanes with double-stranded backbones (LPSQs) [39,40].

POSS have been widely utilized for the fabrication of hydrophobic surfaces and coatings, by virtue of their versatile features and of the possibility to easily covalently link them to polymer backbones [41–45]. In particular, the polyhedral structure and the high number of tunable peripheral functionalities enable us to increase the surface roughness and decrease the surface energy, simultaneously [43–49]. The majority of the studies in the field rely on the synthesis and modification of POSS structures with low-surface energy substituents (e.g., fluoroalkyl, alkyl groups, etc.) and on their exploitation as building blocks or fillers in conjunction with polymers for the production of nanocomposite coatings with improved hydrophobicity [43–45]. However, as already mentioned, the use of fluoroalkyl substituents raises environmental and safety concerns and their substitution with more economical and environmentally friendly materials is required [21].

Concerning the possibility of tuning the roughness with POSS, a few examples can be identified in the literature [47–49]. As an example, Foorginezhad et al. [48] prepared super-hydrophobic coatings by creating a two-layer topography via the spraying method using TiO_2 NPs sols, which impart the micro-roughness, and octavinyl-POSS in polydimethylsiloxane, which delivers nano-roughness and lowers the surface tension thanks to the hydrophobic organic terminations. This approach appears

valuable and simple, but possible NP segregation at the surface has to be considered as source of inhomogeneities and of unintentionally reduced water repellence and mechanical properties.

Apart from cage-like silsesquioxanes, LPSQs have been recently applied in hard coating formulations, profiting from their remarkable thermal properties and processability, and from the enhanced solubility in a wide variety of organic solvents [50–55]. For instance, Lee et al. developed a series of thiol-ene UV-curable inorganic–organic hybrid LPSQs with methacryl and mercaptopropyl functionalities as building blocks of flexible hard coating formulations [56]. These materials exhibited marked pencil hardness in comparison with other organic and multi-formulations and mechanical properties dependent on the peripherical functional groups. Park et al. performed a comprehensive study on the gas transport properties of membranes constituted by LPSQs with different alkyl functionalities [57]. Aside from satisfactory mechanical properties, they found that a combination of larger inter-chain distance and higher side chain rigidity increased the fractional free volume, resulting in a higher gas permeability, while the UV-curing process reduced the permeability of LPSQ due to the restricted chain mobility [57].

According to these studies, the dense polymer structure of UV-curable LPSQs is expected to help in the prevention of water permeation [58]. Finally, though very few information about their wettability properties can be retrieved in the literature, the possibility to introduce hydrophobic and/or UV-curable functionalities (e.g., acrylate or methacrylate groups) make LPSQs suitable candidates for the generation of hard coatings with enhanced thermomechanical durability and hydrophobicity with low environmental and economic costs.

These properties can be further improved by enclosing low loadings of inorganic fillers in the polymer matrix, which may provide tortuous pathways that hinder the possible water permeation, thus further contributing to the water repellence [59–61]. This entails filler homogeneous dispersion and controlled distribution, as well as a careful control of the hybrid interface, which has a significant impact on the structure and mobility of polymer chains and, in turn, on the features of the composites.

Stimulated by this background, in the present study, we consider the possibility of adjusting the thermal properties and wettability of nanocomposite coatings without modifying the surface roughness or the functionalities of silsesquioxanes by simply tuning their interactions at the hybrid interface in a composite system constituted by a LPSQ matrix and suitably functionalized filler NPs. In particular, the idea lies in exploiting the structural rearrangement of the silsesquioxane chains at the interface with the functionalized SiO_2 NPs to enhance the thermal stability and to provide more hydrophobic groups in proximity with the coating surface.

In detail, a fully condensed, ladder-like structured poly(methacryloxypropyl)silsesquioxane with a medium degree of structural regularity (LPMASQ) [52] and SiO_2 NPs functionalized with a methacrylsilane (SiO_2@TMMS) were employed as a suitable matrix and filler, respectively, for producing a nanocomposite by a simple and rapid solvent-casting technique [34]. Among the possible curing approaches, UV curing was selected to achieve crosslinking, leading to cost savings, reducing waste, and assuring a low-temperature treatment. Photo-induced polymerization was monitored using Attenuated Total Reflection Fourier Transform Infrared (ATR FTIR) spectroscopy. The thermal properties of the nanocomposites were evaluated by thermogravimetric analysis (TGA). A comprehensive investigation on the LPMASQ nanocomposites structure and on interactions between the silsesquioxane units and SiO_2 NPs was performed by X-ray diffraction (XRD) and solid-state Nuclear Magnetic Resonance (NMR) spectroscopy. Finally, the surface wettability of the novel nanocomposites was explored through static contact angle (CA) measurements. The results evidenced significant modifications of the structural organization of the LPMASQ backbone as function of silica functionalization, which induce peculiar thermal and hydrophobic features.

2. Experimental

2.1. Materials

Tetraethoxysilane (TEOS), cetyltrimethylammonium bromide (CTAB), 3-methacryloxypropyltrimethoxysilane (TMMS), tetrahydrofuran (THF), K_2CO_3, ethanol, acetone, toluene and Irgacure 651 photoinitiator were purchased from Sigma-Aldrich. Milli-Q water with a resistivity of 18.2 MΩ cm was used.

2.2. Synthesis of LPMASQ

The TMMS-capped LPSQ (LPMASQ) was synthesized via a slightly modified procedure [52].

Briefly, a mixture of K_2CO_3 (0.04 g, 0.29 mmol), distilled water (4.8 g, 0.267 mol) and THF (8 g) was prepared in a 100-mL round-bottomed flask. Next, TMMS (19.9 mL, 0.084 mol) was added to the prepared mixture under nitrogen. The flask was then sealed and left vigorously stirring at room temperature for 10 days. Afterwards, a two-phase mixture was obtained—a colorless aqueous and a cloudy organic one. The organic phase, containing the product, was dissolved in toluene and washed with DI water several times in order to remove the catalyst. Subsequently, $MgSO_4$ was added in order to eliminate traces of water. The organic phase, as obtained, was then put under a vacuum in order to eliminate the toluene and a transparent oil-like product was obtained.

2.3. Synthesis of Naked Silica NPs

Silica NPs were synthetized via a sol–gel route according to a slightly modified method already reported in the literature [62]. Briefly, 4 g of CTAB was dissolved in NaOH solution (14 mL, 2 M) and 1920 mL of Milli-Q water at 60 °C. After 45 min of stirring, TEOS (24 mL) was added and the reaction was left in this condition for 2 h. Afterwards, the white powder was separated by filtration and re-dispersed under stirring for 20 h at 60 °C in HCl solution (40 mL, 36 wt.%) end ethanol (300 mL) in order to eliminate the CTAB template. Then, the precipitated silica was separated by centrifugation and washed with DI water until pH 7.0 ± 0.2 was reached. Finally, silica NPs were filtered and dried in an oven at 80 °C for 24 h.

2.4. Synthesis of TMMS Functionalized Silica NPs

Silica NPs, as previously prepared, were functionalized with TMMS following the procedure proposed by [35]. (Scheme 1). In a functionalization procedure, 0.5 g of silica NPs was dispersed in 20 mL of toluene by sonication (30 min). TMMS (0.5 mL) was added dropwise and the mixture, as prepared, was brought to 120 °C and stirred for 10 h.
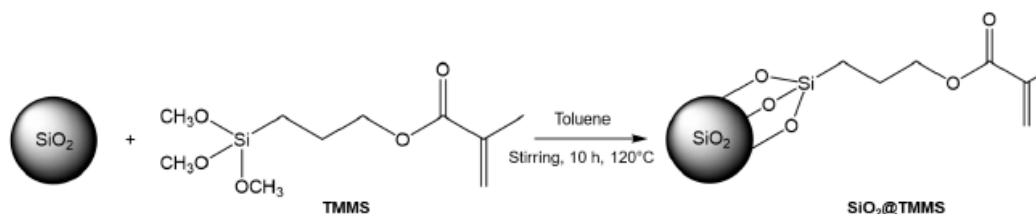

Scheme 1. Procedure for silica nanoparticle (NP) functionalization with TMMS.

The solid was then separated by centrifugation (9000 rpm), washed several times with toluene and acetone in order to eliminate traces of non-reacted silane and dried overnight at 80 °C.

2.5. Preparation of LPMASQ Nanocomposites

For the preparation of LPMASQ nanocomposites, a solvent casting technique was utilized (Scheme 2). Three different samples were prepared, namely homopolymerized LPMASQ (h-LPMASQ), SiO_2/LPMASQ and SiO_2@TMMS/LPMASQ.
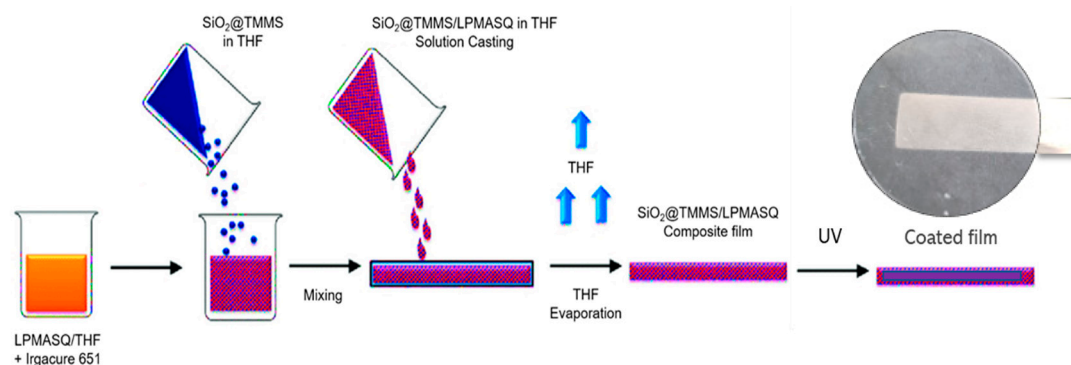
Scheme 2. Nanocomposites preparation by solution casting, followed by UV-induced crosslinking.

In detail, for h-LPMASQ, 2 g of LPMASQ was dissolved in 2 mL of THF and 1 mL of a solution of Irgacure 651 (20 mg in 1 mL THF) was added under stirring. In the case of SiO_2/LPMASQ and SiO_2@TMMS/LPMASQ, 100 mg of SiO_2 or SiO_2@TMMS (5 wt.% on LPMASQ) were dispersed in 2 mL of THF by sonication; then, 1 mL of a solution of Irgacure 651 (20 mg in 1 mL THF) was added. Finally, 2 g of LPMASQ were dissolved and the solutions were cast in Polyethylene (PE) Petri dishes ($\emptyset$ = 8 cm). After THF evaporation at room temperature for 3 h, nanocomposites were irradiated with a UV lamp (125 W, irradiance 1 mW/cm^2) for 5 min under N_2 in order to obtain crosslinked materials. To provide a comprehensive characterization, nanocomposites were peeled from the PE substrate, resulting in self-standing film with an average thickness of 280–300 μm (see SEM characterization).

2.6. Characterizations

Fourier Transform Infrared Spectroscopy (FTIR) spectra of SiO_2@TMMS nanopowders were acquired by a PerkinElmer Spectrum 100 instrument in Attenuated Total Reflection (ATR) mode in the spectral region 4000–650 cm^{-1}, with a resolution of 1 cm^{-1}.

Scanning electron microscopy (SEM) images on both silica NPs and composites were collected by a Vega TS5136 XM Tescan microscope in a high-vacuum configuration. The electron beam excitation was 30 kV at a beam current of 25 pA, and the working distance was 12 mm. In this configuration, the beam spot was 38 nm. The average diameter of SiO_2 NPs was evaluated by measuring the sizes of ~100 particles in SEM images.

Nitrogen physisorption experiments on SiO_2 NPs were performed by using a Micromeritics ASAP2020 instrument, after evacuation of the samples at 180 °C overnight. A liquid N_2 bath was used for measurements at 77 K. Specific surface area values (SSA_{BET}) were determined by the Brunauer–Emmett–Teller (BET) method, while pore size distribution was calculated by the Barret–Joyner–Halenda (BJH) method.

XRD patterns were collected on the composites with a Brucker D8 Advance (Cu K_α radiation) in the range 20–70° 2θ (2θ step 0.025°, count time of 2 s per step).

TGA thermograms were collected by using a Mettler Toledo TGA/DSC1 STARe system at a constant gas flow (50 cm^3·min^{-1}). The sample powders were heated in air from 30 to 1000 °C at a rate of 10 °C·min^{-1}.

Liquid-state ^{1}H-NMR analyses were performed on pristine LPMASQ dissolved in CDCl$_3$ by a Bruker Avance 400 WB spectrometer operating at a proton frequency of 400.13 MHz.

Solid-state NMR analyses were carried out with a Bruker 400 WB spectrometer operating at a proton frequency of 400.13 MHz. The experiments were run on homo-polymerized LPMASQ and on silica/LPMASQ nanocomposites obtained after irradiation. NMR spectra were acquired with cp and sp pulse sequences under the following conditions: ^{13}C frequency—100.48 MHz, contact time—2 ms, decoupling length—5.9 μs, recycle delay—5 s, 2 k scans. ^{29}Si frequency: 79.48 MHz, contact time—5 ms, decoupling length—6.3 μs, recycle delay—10 s, 2 k scans; single pulse sequence—π/4 pulse 3.9μs, recycle delay—45 s, 2 k scans. Samples were packed in 4-mm zirconia rotors, which were spun at 8 kHz under air flow. Adamantane and Q_8M_8 were used as external secondary references.

Polymerization under UV light was monitored using ATR FTIR spectroscopy. The spectra were acquired with a Nicolet iS50 spectrometer (Thermo Fisher Scientific Inc., Waltham, MA, USA), equipped with a Nicolet™ Smart iTX accessory (with diamond crystal). Spectra were recorded in the 650–4000 cm^{-1} range, with 1 scan per spectrum and a resolution of 4 cm^{-1}. The methacrylate double-bond conversion was estimated through the absorbance of the band at 1638 cm^{-1}, using the following Equation:

$$Conversion\%_{t=x} = 100 \times \left(1 - \frac{A_{t=x}}{A_{t=0}}\right)$$

Surface wetting properties were characterized by contact angle measurements on the air side of the obtained nanocomposites, by means of the sessile drop method (OCA 15, DataPhysics Instruments GmbH, Filderstadt, Germany) using deionized water as the testing liquid. In particular, we did not only measure the static contact angle, θ, formed by a drop gently deposited on the surface, but also the advancing, $θ_A$, and receding, $θ_R$, contact angles, which are measured by quasi-statically expanding and contracting the drop volume on a horizontal surface. The difference between the two angles, $Δθ = θ_A - θ_R$, is known as contact angle hysteresis. As highlighted in the literature [63,64], it is more appropriate to provide a range for the contact angles (i.e., $θ_A$, $θ_R$, and $Δθ$) rather than a single value for the contact angle, to supply a more a complete description of the wetting properties: $θ_A$, $θ_R$, and $Δθ$ are related to drop capillary adhesion force, and thus drop mobility on a solid surface [65]. During experiments, a water drop with a volume of 3 μl was initially deposited on the surface. After the drop came to rest, the water was first infused to increase the drop volume (up to 8 μL, with an infusion rate of 0.2 μL/s) and then extracted to decrease the volume, enabling the measurement of $θ_A$ and $θ_R$.

3. Results and Discussion

The idea to produce nanocomposites with improved thermal properties and hydrophobicity relies on the effect of SiO_2 and SiO_2@TMMS incorporation on the structure/molecular architecture of the LPMASQ chains. In this regard, the characterizations of precursor materials were first performed, followed by those of the nanocomposites.

3.1. Characterization of Pristine LPMASQ

To preliminary compare the chemical structure of the obtained LPMASQ to that reported in the literature, FTIR and liquid-state NMR analyses were performed (Figure 1). The obtained material has the same structural characteristics of the systems reported in [51,52], and it belongs to the "medium-degree regular" category of LPSQs, if compared to highly regular template-route phenyl–LPMASQ [53] or to phenyl–silsequioxane resins with different degrees of ordering [54]. Thus, a dominant ladder-like structure can be expected, while some structural irregularity in combination with flexible substituents favor its remarkable solubility in THF.
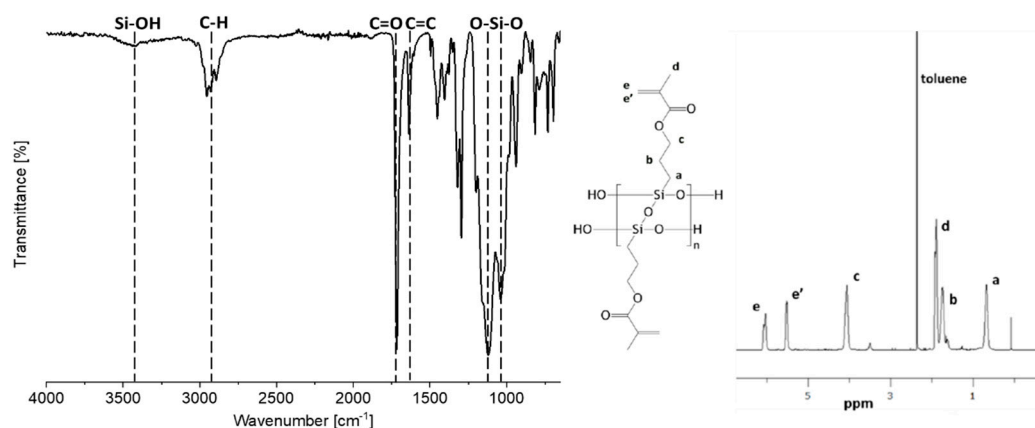
Figure 1. FTIR (**a**) and ^{1}H NMR (**b**) spectra of LPMASQ.

3.2. Pristine SiO$_2$ and SiO$_2$@TMMS NPs Characterization

The morphology of naked silica particles was preliminarily inspected by SEM microscopy (Figure 2a). In detail, SEM micrographs show the presence of silica nanospheres (inset Figure 2a) with an average diameter of 189 ± 32 nm. Nitrogen physisorption experiments revealed that SiO$_2$ NPs show a type IV Brunauer isotherm (Figure 2b) with a very narrow hysteresis loop. The BET surface area was 691 ± 5 m^2/g, while the BJH pore size distribution (inset Figure 2b) revealed that the mesopore size corresponds to the silica's intrinsic mesoporosity.
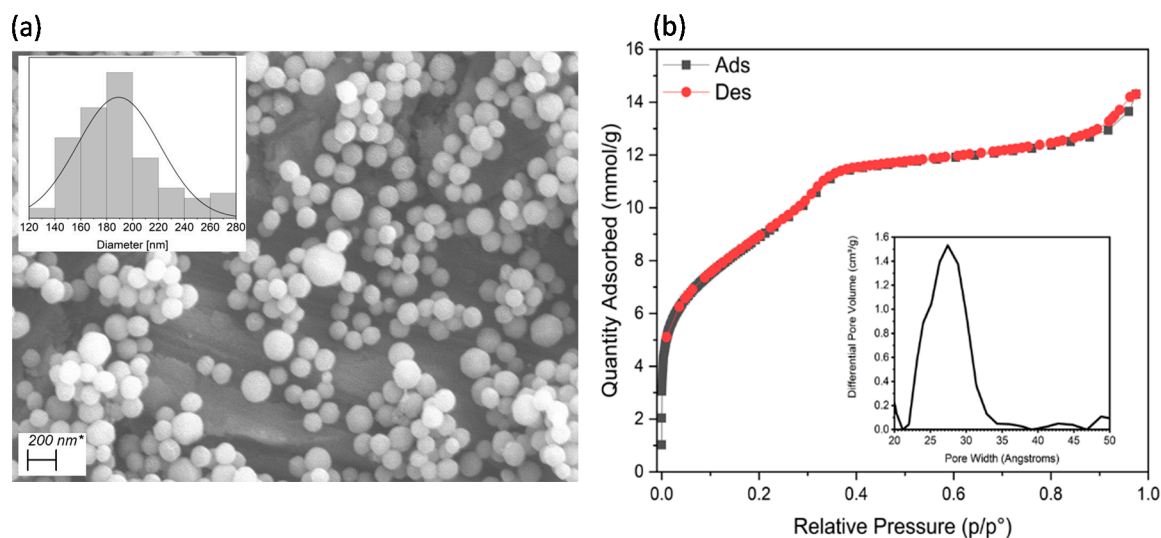

Figure 2. Characterization of naked SiO$_2$ NPs: (**a**) SEM micrographs with particle size distribution in the inset; (**b**) adsorption/desorption isotherm at liquid nitrogen temperature and pore size distribution.

Silica NPs and TMMS-functionalized silica (SiO$_2$@TMMS) were further characterized by ATR-FTIR and TGA.

Figure 3a reports the comparison among the spectra of pure TMMS, SiO$_2$ and SiO$_2$@TMMS NPs. As already reported, the spectrum of TMMS shows the following main bands (Figure 3a, green line): the silane C−H stretching at 2940 and 2840 cm^{-1}; the intense carbonyl vibration of non-hydrolyzed TMMS at 1715 cm^{-1} and the weak stretching of C=C bond at 1635 cm^{-1}; the methylene C−H bending at 1454 cm^{-1}; the −C−CO−O− skeletal vibration from the methacryloxy group at 1320 and 1210 cm^{-1}; the band of ν Si–O–C at 1080 cm^{-1}. For unmodified SiO$_2$ (Figure 3a, black line), the following can be seen: the very broad absorption between 3600–3200 cm^{-1} is attributable to the stretching of OH groups from physically absorbed water; the tiny peaks in the region at 1698 and 1633 cm^{-1} are ascribed to

CTAB residues and to water scissoring, respectively; finally, the vibrations at 1090 and 960cm^{-1} belong to the Si–O–Si and to Si–OH stretching, respectively.
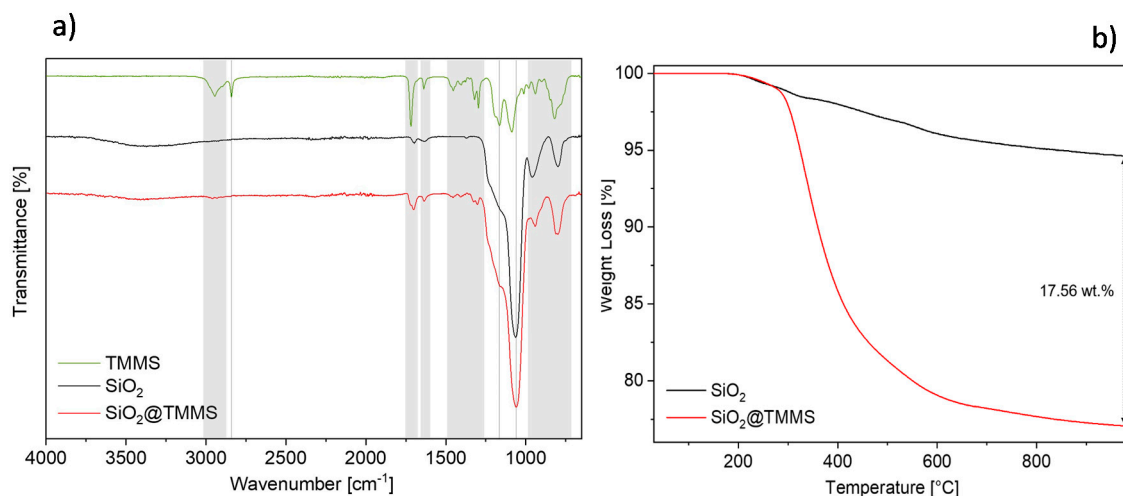

Figure 3. (**a**) FTIR spectra of pure TMMS (green line), naked SiO$_2$ (black line) and SiO$_2$@TMMS NPs (red line); (**b**) thermogravimetric analysis (TGA) curves of SiO$_2$ (black line) and SiO$_2$@TMMS NPs (red line).

In the case of SiO$_2$@TMMS (red line in Figure 3a), the very weak peak in the region 3000–2922 cm^{-1} belongs to the C-H asymmetric stretching vibrations of the methyl groups. The occurrence of characteristic bands of vibrational stretching C=O (1717 cm^{-1}) and C=C (1636 cm^{-1}) indicate the presence of methacrylate functional groups in the SiO$_2$@TMMS spectrum. The peaks in the region 1500–1250 cm^{-1} are affiliated to the symmetric deformation bending of C–H and to the vibration from the methacryloxy group. Finally, the absence of a peak at 2840 cm^{-1}, corresponding to the Si-O-CH$_3$, and the depletion of the Si–OH stretching at 960 cm^{-1} demonstrates the grafting of TMMS at the silica surface. To quantitatively assess the TMMS functionalization degree, TGA analysis was performed on SiO$_2$@TMMS and on naked silica NPs (Figure 3b). The total amount of TMMS grafted onto SiO$_2$ corresponds to ~17.6 wt.% and was evaluated by the net weight loss of SiO$_2$@TMMS between 180 and 980 °C, i.e., considering the total weight loss with the exclusion of that associated to bare SiO$_2$.

3.3. Characterization of LPMASQ Nanocomposites

Nanocomposites were prepared by solution casting, followed by irradiation, to induce the polymerization of the methacrylic double bonds: quasi-transparent films were obtained, which could be detached from the substrate, although fragile. The double bond conversion was measured by ATR-FTIR. As an example, Figure 4 shows the spectra of sample SiO$_2$/LPMASQ before and after irradiation; the spectra of the sample after irradiation are recorded on both sides, after peeling off the coating, i.e., the side in contact with the substrate used for casting and the air surface.
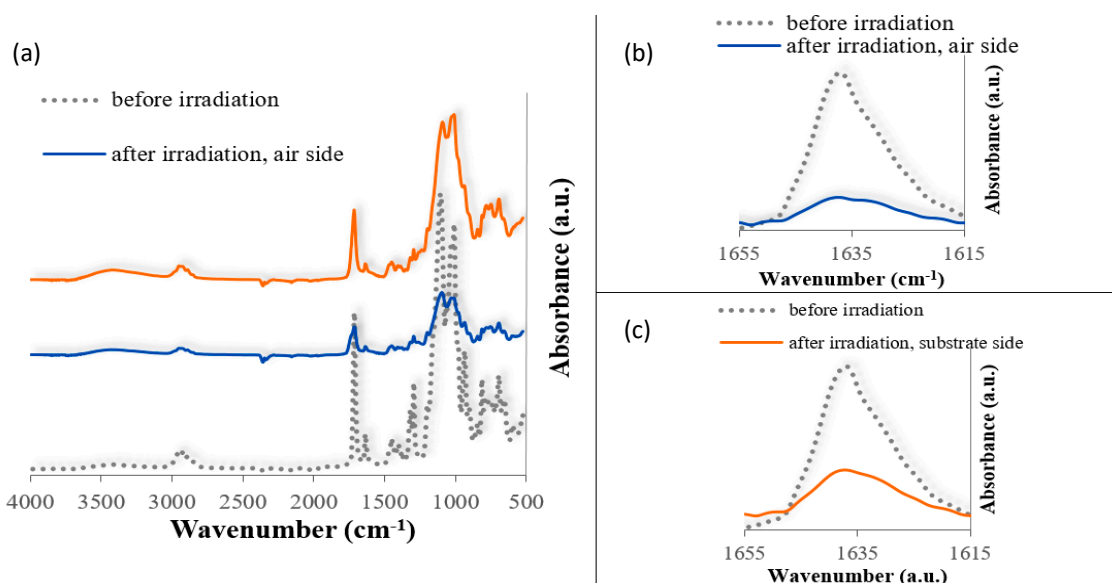
Figure 4. (**a**) Attenuated Total Reflection (ATR)-FTIR spectra of SiO$_2$/LPMASQ sample before and after irradiation. (**b**) magnification of the methacryl band region of SiO$_2$/LPMASQ spectra recorded on the air side; (**c**) magnification of the methacryl band region of SiO$_2$/LPMASQ spectra recorded on the substrate side.

When evaluating the absorbance of the vibrational band of the methacrylic groups (shown in Figure 4b,c, the conversion of the polymerization reaction under light was estimated. The values are gathered in Table 1. Conversion η on the air side is quite high for the neat LPMASQ and decreases with the addition of silica nanoparticles; on the opposite side, due to the light absorbance along the thickness of the film, the conversion is smaller. Thus, due to the light intensity gradient, there is a conversion gradient. If an average conversion is estimated as the average value of the air side and substrate side conversion, a rough evaluation of the ratio between the polymer and the unreacted monomer can be made using η/1 − η.

Table 1. Double bond conversion.

Sample	Conversion η Air Side%	Conversion η Substrate Side%	Polymer/Unreacted Monomer(η/1 − η)
h-LPMASQ	87	55	2.5
SiO$_2$/LPMASQ	75	51	1.7
SiO$_2$@TMMS/LPMASQ	68	63	1.9

Apart from a preliminary visual inspection, the surface morphologies of the samples were investigated by SEM microscopy (Figure 5). In the case of h-LPMASQ, no surface features were detected. Upon the incorporation of naked SiO$_2$ NPs, partial segregation effects occur and aggregated structures can be observed, expected considering the intrinsically low affinity between LMPASQ chains and hydrophilic silica filler (Figure 5a). Instead, more homogeneous surfaces can be observed in the case of SiO$_2$@TMMS/LPMASQ (Figure 5b), where the silica functionalization probably promotes an improved compatibilization and distribution of the filler in the silsesquioxane matrix. SEM cross section images reveal that the thickness of the nanocomposites lies between 280 and 300 μm (Figure 5c,d).
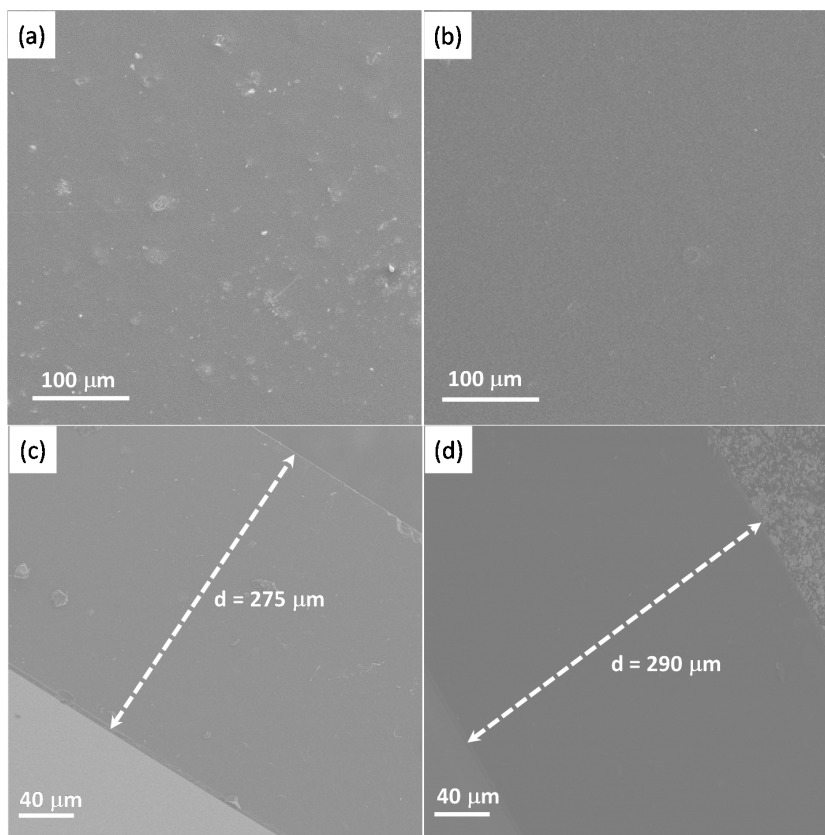
Figure 5. SEM micrographs of (**a**) SiO$_2$/LPMASQ and (**b**) SiO$_2$@TMMS/LPMASQ nanocomposites (**c**) and (**d**) cross section images of SiO$_2$/LPMASQ and SiO$_2$@TMMS/LPMAS, respectively.

The effect of the incorporation of SiO$_2$ and SiO$_2$@TMMS on h-LPMASQ properties was evaluated by TGA (Figure 6). All the samples show a substantial single-step degradation, which very slightly moves to higher temperatures in the case of SiO$_2$/LPMASQ. Instead, for the SiO$_2$@TMMS/LPMASQ composite, a significant increase (about 30 °C) in thermal stability is observed compared to the other samples.

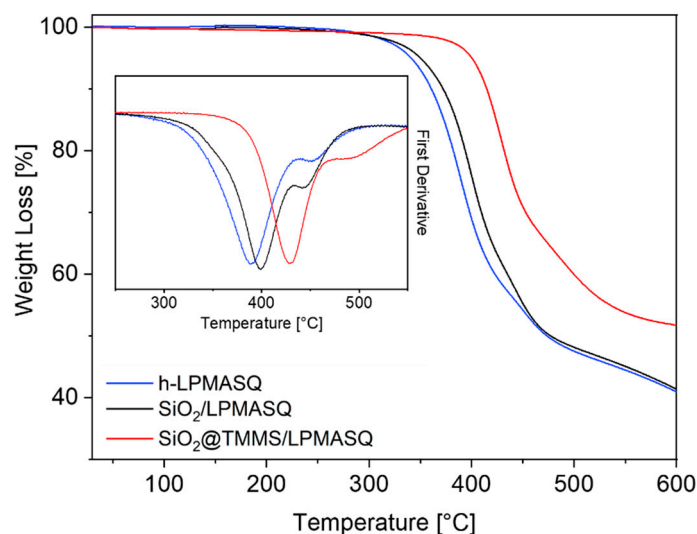**Figure 6.** Thermograms of h-LPMASQ (blue line), SiO$_2$/LPMASQ (black line) and SiO$_2$@TMMS/LPMASQ (red line) nanocomposites; inset shows the corresponding first derivative of the TGA curves (first derivative thermogravimetric curves, DTG).

This suggests that the interactions at the hybrid interface between the organically modified silica and the silsesquioxanes functionalities effectively promote the thermal stability.

To examine the bulk structure of both h-LPMASQ and nanocomposites in depth, XRD analyses were carried out (Figure 7). As extensively reported in the literature [66], LPMASQ (blue line in Figure 7) displays a diffraction pattern constituted by two main amorphous "halo" at room temperature. The former, located at $2\theta \sim 6°$, is associated to the intramolecular periodic chain-to-chain distance (denoted as Y in inset of Figure 7). The second peak at $2\theta \sim 20°$ refers instead to the average thickness X of the Si–O–Si silsesquioxane structure.
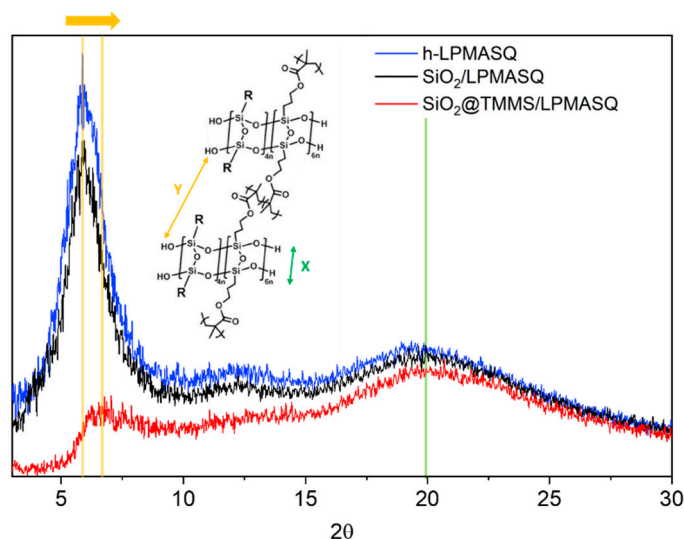

Figure 7. XRD pattern of h-LPMASQ (blue line) SiO_2/LPMASQ (black line) and SiO_2@TMMS/LPMASQ (red line) nanocomposites; inset shows schematic structure of LPMASQ backbone and the X and Y distances.

A third, very weak and broad reflection can be detected at $2\theta \sim 12.3°$, which is not reported in the literature. The origin of this halo may be tentatively ascribed to the distance generated by the intrachain interaction occurring upon UV-induced photopolymerization.

Analyses of XRD patterns revealed that the chain-to-chain distance remains unaffected upon introduction of naked SiO_2 NPs (i.e., SiO_2/LPMASQ composite), while it slightly decreases from 14.9 Å to 13.1 Å in SiO_2@TMMS/LPMASQ composite (see Table 2). The average thickness of the ladder-like siloxane backbone does not show any appreciable variation. These results suggest a structural modification of the siloxane backbone induced by the incorporation of SiO_2@TMMS NPs, probably connected to the interaction between the methacrylate functionalities of TMMS and those of LPMASQ.

Table 2. XRD parameters of diffractograms reported in Figure 6.

Sample	Diffraction Peak (2θ)	d-Spacing (Å)
h-LPMASQ	5.94	14.9
SiO_2/LPMASQ	5.94	14.9
SiO_2@TMMS/LPMASQ	6.74	13.1
all	20.08	4.4

A deeper understanding of how the silsesquioxane units are modified by the filler introduction was achieved by various ^{13}C and ^{29}Si solid-state NMR experiments.

The ^{13}C Cross Polarization/Magic Angle Spinning (CPMAS) spectra of h-LPMASQ and LPMASQ/silica nanocomposites after irradiation are shown in Figure 8, together with the structural scheme and C labeling used for peak assignment [67].
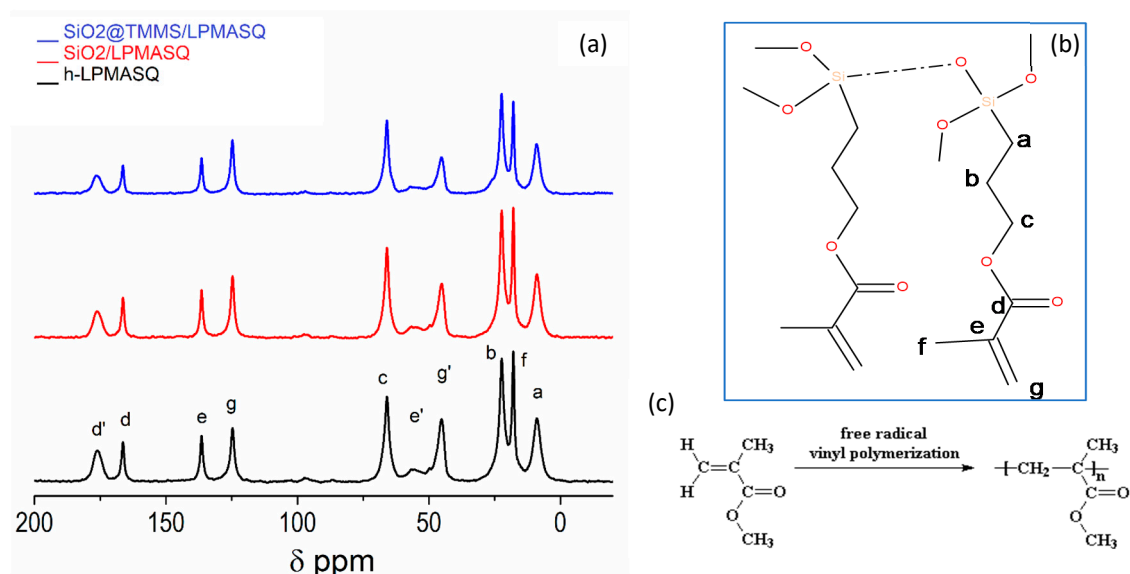

Figure 8. (**a**) ^{13}C CPMAS spectra of h-LPMASQ (black line), SiO$_2$/LPMASQ (red line) and SiO$_2$@TMMS/LPMASQ (blue line). The LPMASQ structure with C labeling and the polymerization scheme [68] are shown in figures (**b**) and (**c**), respectively.

The LPMASQ skeleton (black curve) is characterized by the three resonances due to the methylene carbon atoms in the propyl chain (a, b, c) and the three resonances of the methacrylate tail, i.e., carbonyl (d, 165 ppm), vinyl (e and g at 135 and 124 ppm respectively) and methyl (f) C atoms [68]. The UV-induced crosslinking of the LPMASQ units is demonstrated by the appearance of both the methylene peaks in the region 40–60 ppm (e', g') and by the second downfield shifted carbonyl resonance at 175 ppm (d'), which result from the partial consumption of the methacrylate vinyl bonds (signals e and g). It can be noticed that these additional peaks are characterized by a wider linewidth. As the signal linewidth is inversely proportional to the functional group mobility, it can be inferred that d', e' and g' signals represent more rigid structures with respect to the free methacrylate ends, further proving a network formation.

The spectra of LPMASQ enclosing both SiO$_2$ and SiO$_2$@TMMS display similar features (red and blue curves). The contribution of TMMS units to the SiO$_2$@TMMS/LPMASQ spectrum cannot be detected since it is too weak and the related signals perfectly overlap with those of LPMASQ.

It is interesting to note that, given the presence of both d and d' signals, it is possible to calculate the extent of the photoinduced polymerization reaction taking place through the methacrylic double bonds, since the CPMAS experimental conditions have been selected in order to give the maximum intensity of both signals: the ratio d'/d corresponds to the ratio between the polymer and the monomer. The obtained values summarized in Table 3 show that the silica presence determines a slight decrease in the extent of silsesquioxane methacrylic bond polymerization.

Table 3. Extent of LPMASQ polymerization, calculated from the C=O area as the ratio d'/d.

Sample	d'/d
h-LPMASQ	67.2/32.8 = 2.1
SiO$_2$/LPMASQ	61.2/38.8 = 1.6
SiO$_2$@TMMS/LPMASQ	61.3/38.7 = 1.6

The data are in good agreement with the values obtained by processing the conversion values η obtained from the ATR-FTIR measurements.

The inorganic network can be exhaustively described through the analysis of the ^{29}Si CPMAS NMR spectra (Figure 9). The NMR signals are labeled according to the usual nomenclature where T^n and Q^n refer to R-Si(OSi)$_n$(OH)$_{3-n}$ and to Si(OSi)$_n$(OH)$_{4-n}$ units, respectively. Figure 9a presents a comparison of the spectra of h-LPMASQ and nanocomposites.

| (a) | (b) |

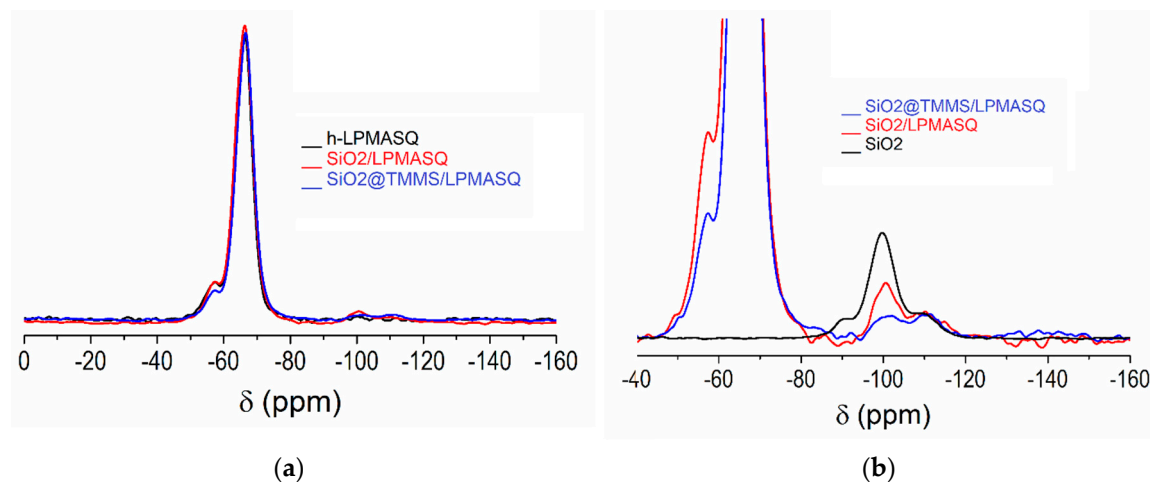**Figure 9.** ^{29}Si CPMAS spectra of (**a**) h-LPMASQ (black line), SiO$_2$/LPMASQ (red line), and SiO$_2$@TMMS/LPMASQ (blue line), normalized on the T^3 peak, and (**b**) magnification of the Q unit region of the silica-based composites normalized on the Q^4 peak; the silicon-29 spectrum of pristine SiO$_2$ particles (black line) is also shown.

The inorganic network of LPMASQ is characterized by about 93% of fully condensed T^3 units (at −66.4 ppm), with a minor amount of terminal T^2 units (peak at −57.1 ppm), in agreement with previous findings [52]. The presence of filler in the nanocomposites is proven by the peaks in the Q region (Figure 9b): the resonance at −110.4 refers to the Q^4 units [Si(OSi)$_4$] and the one at −100.0 ppm to the surface Q^3 sites [Si(OSi)$_3$OH]. The black curve of Figure 9b represents the pristine silica filler. It is characterized by three structural units Q^4, Q^3 e Q^2 (the latter at −90.0 ppm).

From a qualitative inspection, it can be noticed that the spectral features of both LPMASQ and SiO$_2$ slightly change in the nanocomposites and these effects seem related to both silica functionalization and amount. The modification at the expense of the silsesquioxane skeleton is almost negligible in the case of nanocomposites enclosing naked SiO$_2$ NPs, whereas the addition of the functionalized filler reduces the end chain sites T^2.

Conversely, the silica filler is subjected to an increase in the condensation degree, as clearly shown by the reduction in Q^2 and Q^3 resonances. This can be ascribed to the partial co-condensation of silanol groups with those of LPMASQ, in agreement with the observed decrease in the T^2 units. This effect is more relevant for SiO$_2$@TMMS/LPMASQ, where, probably, the consumption of Si-OH is also connected to the TMMS functionalization.

The quantitative analysis, obtained through the recording of the ^{29}Si MAS spectra, as well as confirming the trend for T^2 described above, reveals a variation in the T^3 line shape among the samples (Figure 10, left). In particular, the profile fitting unveils the presence of two T^3 components at −64 ppm and −67 ppm, respectively, whose relative contribution depends on the silica functionalization. In detail, a partial reduction in the percentage of downfield components can be observed, which becomes more significant for SiO$_2$@TMMS/LPMASQ (Table 4).

(a)　　　　　　　　　　　　　　　　　　　　　　(b)
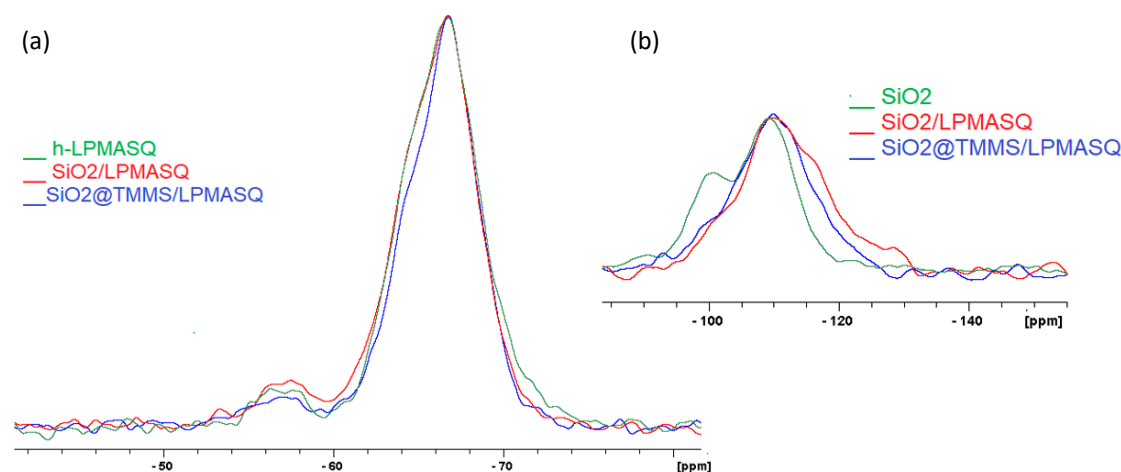

Figure 10. Details of ^{29}Si Magic Angle Spinning (MAS) spectra of h-LPMASQ (green), SiO$_2$/LPMASQ (red line), and SiO$_2$@TMMS/LPMASQ (blue line) normalized on the T^3 peak (**a**), and of the Q unit region normalized on the Q^4 peak (**b**). Here pristine SiO$_2$ particles spectrum (green line) is given for the sake of comparison.

Table 4. Quantitative analysis obtained through the profile fitting of T^3 resonance with two components. The amount (%) of every component and the related half linewidth (LW/2) are reported. Confidence level >95%.

Sample	Signal at −64,0 ppm		Signal at −66,9 ppm	
	%	LW/2*	%	LW/2*
h-LPMASQ	25.8	132.8	74.2	161.6
SiO$_2$/LPMASQ	24.2	129.3	75.8	156.8
SiO$_2$@TMMS/LPMASQ	22.3	127.8	77.7	150.0

Moreover, a change in the half width at half height (LW/2) of both the components is noticeable in the nanocomposites. It has been shown in the literature that the LW/2 of T^3 peak is inversely proportional to the polymer skeleton regularity. As summarized by Seki et al. [69], low molecular weight PSQs are characterized by LW/2 of 240–300 Hz, whereas highly ordered long ladder structures reduce the LW/2 to about 150 Hz and present a chemical shift (δ) of about −65 ppm. A slight upfield of the chemical shift (up to −67 ppm) and larger LW/2 were attributed to structural defects and cage structures [50]. Accordingly, the results on our samples support the description of long ordered ladder structures with the presence of irregularities, as also indicated by TGA and XRD results.

Interestingly, a reduction in LW/2 for both the T^3 components is observed, notably in the presence of SiO$_2$@TMMS. This again reflects the possibility of an ordering of the LPMASQ chains, supporting the hypothesis of a rearrangement of the silsesquioxane skeleton around the functionalized silica particles.

The interpretation is also endorsed by the small high-field broadening of the Q^4 component observed in the spectra of SiO$_2$/LPMASQ and SiO$_2$@TMMS/LPMASQ (Figure 10, right). According to Density Functional Theory (DFT) calculations, this effect can be attributed to the contribution of Q^4 units with distorted (wider) bond angles [70].

In conclusion, the NMR results highlight a conformational modification of the LPMASQ induced by silica NPs, which is mediated by the filler–silsesquioxane interface and probably explains the different thermal stabilities of the composite materials.

Wettability tests were carried out to provide a proof of concept about the possibility to exploit the structural rearrangement of the silsesquioxane chains at the interface with the SiO$_2$ filler to adjust the hydrophobicity of nanocomposite coatings. Measurements were performed only on the air side of the films as detachment from the substrate caused some damage to the lower surface, mostly due to the good adhesion of the material onto the substrate.

The results of contact angle measurements and water droplet profiles of LPMASQ nanocomposites are summarized in Figure 11. For all samples, θ_A is approximately constant (in the range 90°–93°), denoting a moderate hydrophobicity, with significant variations observed for θ_R and thus $\Delta\theta$. For h-LPMASQ, θ_R is equal to 59°, with a hysteresis $\Delta\theta = 31°$. The hysteresis is relatively high, denoting a high liquid–substrate adhesion. With SiO$_2$ NP inclusion (SiO$_2$/LPMASQ sample), θ_R decreases, leading to an increase in the hysteresis, $\Delta\theta$. This can be associated to the surface segregation effects observed in some regions of SiO$_2$/LPMASQ samples, as visible from the SEM images (Figure 5), which enhance the hydrophilicity, thus reducing the water repellence.
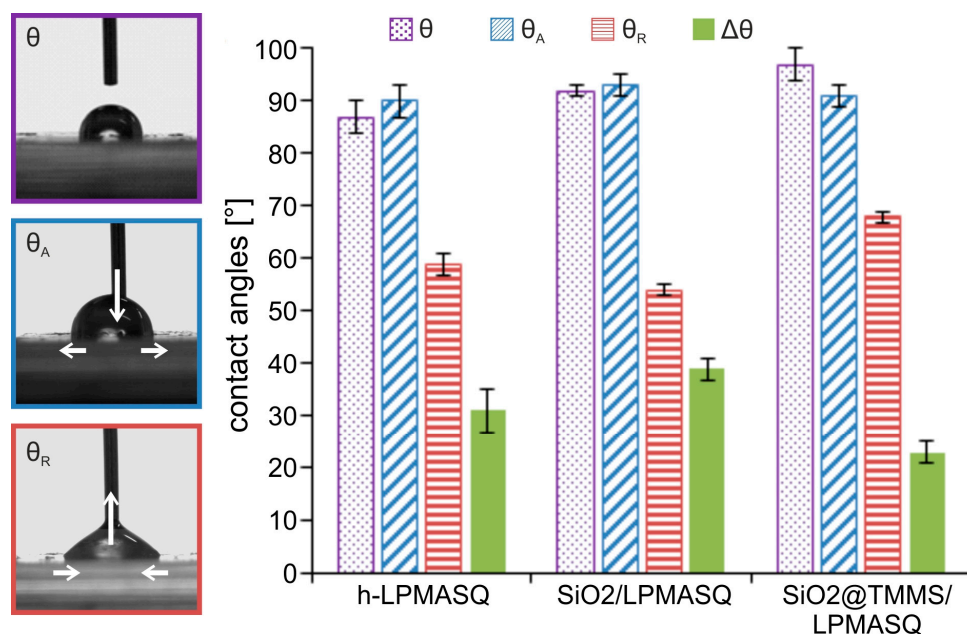

Figure 11. Contact angle values for LPMASQ, SiO$_2$/LPMASQ and SiO$_2$@TMMS/LPMASQ surfaces. Images on the left are representative snapshots showing the evaluation of the static, θ (top), the advancing, θ_A (center), and the receding, θ_R (bottom), contact angles. The contact angle hysteresis is calculated as $\Delta\theta = \theta_A - \theta_R$.

Interestingly, in SiO$_2$@TMMS/LPMASQ, θ_R increases, and since θ_A is constant, the hysteresis, $\Delta\theta$, decreases to a minimum value of 24°. This suggests that the highest hydrophobicity of the sample results from the rearrangement of silsesquioxane chains at the interface with the silica filler, as predicted by XRD and more clearly depicted by NMR.

Finally, it has to be pointed out that contact angle measurements confirm that particle-loaded coatings can still be considered smooth, from a wetting perspective, since neither a Wenzel state (i.e., significant increase in contact angle hysteresis) nor a Cassie–Baxter state (i.e., superhydrophobic wetting state) are observed. This result is not unexpected, since silsesquioxane-based polymer nanocomposites display smooth surfaces in general [71,72].

Moreover, according to the literature, an average roughness $R_a < 100$ nm generally has a slight influence on contact angles and hysteresis [73–75]. Thus, though we cannot exclude an increase in surface roughness upon the introduction of silica NPs in LPMASQ, the effect appears negligible and, especially in the case of SiO$_2$@TMMS filler, cannot be invoked to explain the decreased wettability of the obtained coating surfaces.

Instead, we can infer that the increase in hydrophobicity in SiO$_2$@TMMS/LPMASQ is likely related to the surface enrichment of low-surface tension silsesquioxane terminations as a consequence of the re-organization of LPMASQ chains upon interaction with the silica fillers.

4. Conclusions

In this study, we considered the possibility of adjusting the hydrophobicity and the thermal resistance of nanocomposite coatings without modifying the surface roughness or the functionalities of silsesquioxanes by simply tuning their interactions at the hybrid interface in a composite system constituted by a LPSQ matrix and suitably functionalized silica NPs as the filler.

An UV-curable ladder-like structured poly (methacryloxypropyl) silsesquioxane (LPMASQ) was used, since it affords advantageous properties, like superior thermal properties and processability, and enhanced solubility in a wide variety of organic solvents. Moreover, the dense polymer structure was expected to help in the prevention of water permeation. SiO_2 NPs were functionalized with a methacrylsilane (SiO_2@TMMS), in order to grant both filler homogeneous dispersion and, upon UV-curing, desired interactions with the silsesquioxane terminations.

The effects of the filler surface functionalization on the structure of the polymeric chains and, in turn, on the wetting features of the resulting materials, were carefully investigated, in view of their potential application in protective coatings.

In detail, SEM investigation revealed that the nanocomposites have a thickness of 280–300 μm and generally homogeneous surfaces. However, when naked silica NPs are utilized as the filler, some aggregations become visible. TGA thermograms show a single-step degradation for all the samples with an appreciable increase in the thermal stability only for SiO_2@TMMS/LPMASQ. Accordingly, XRD analysis revealed a structural modification of the siloxane backbone by the incorporation of SiO_2@TMMS NPs, envisaging interactions between the organically modified silica and the silsesquioxane functionalities.

Solid-state NMR investigation supports this hypothesis, evidencing conformational alterations of the LPMASQ structure induced by the introduction of silica NPs. In particular, in SiO_2@TMMS/LPMASQ nanocomposites, an ordering of the LPMASQ chains is observed, indicating a rearrangement of the silsesquioxane skeleton around the functionalized filler particles.

This surface-mediated evolution of the LPMASQ molecular structure results in a more significant increase in the hydrophobicity for SiO_2@TMMS/LPMASQ in comparison to the other nanocomposites, suggesting that tailoring the interactions at the hybrid interface between the filler and LPSQ may be a promising alternative to obtain coatings with tunable wettability.

References

1. Available online: https://www.businesswire.com/news/home/20190419005029/en/ (accessed on 20 May 2020).
2. Kalyani, T.N.; Dhoble, S.J. Novel materials for fabrication and encapsulation of OLEDs. *Renew. Sustain. Energy Rev.* **2015**, *44*, 319–347. [CrossRef]
3. Giannouli, M.; Drakonakis, V.M.; Savva, A.; Eleftheriou, P.; Florides, G.; Choulis, S.A. Methods for improving the lifetime performance of organic photovoltaics with low-costing encapsulation. *ChemPhysChem* **2015**, *16*, 1134–1154. [CrossRef]

4.   Burrows, P.E.; Bulovic, V.; Forrest, S.R.; Sapochak, L.S.; Mccarty, D.M.; Thompson, M.E. Reliability and degradation of organic light emitting devices. *Appl. Phys. Lett.* **1994**, *65*, 2922–2924. [CrossRef]

5.   Yüce, M.Y.; Demirel, A.L.; Menzel, F. Tuning the surface hydrophobicity of polymer/nanoparticle composite films in the wenzel regime by composition. *Langmuir* **2005**, *21*, 5073–5078. [CrossRef] [PubMed]

6.   Kessler, D.; Theato, P. Reactive surface coatings based on polysilsesquioxanes: Defined adjustment of surface wettability. *Langmuir* **2009**, *25*, 14200–14206. [CrossRef] [PubMed]

7.   Saber, I.; Maha, S. Superhydrophobic coating polymer/silica nanocomposites: Part I synthesis and characterization as eco-friendly coating. *Silicon* **2020**, *12*, 805–811.

8.   Ahmed, N.; Fan, H.; Dubois, P.; Zhang, X.; Fahad, S.; Aziz, T.; Wan, J.J. Nano-engineering and micromolecular science of polysilsesquioxane materials and their emerging applications. *Mater. Chem. A* **2019**, *7*, 21577–21604. [CrossRef]

9.   Fahlteich, J.; Fahland, M.; Schönberger, W.; Schiller, N. Permeation barrier properties of thin oxide films on flexible polymer substrates. *Thin Solid Films* **2009**, *517*, 3075–3080. [CrossRef]

10.   Charton, C.; Schiller, N.; Fahland, M.; Holla, A. Development of high barrier films on flexible polymer substrates. *Thin Solid Films* **2006**, *502*, 99–103. [CrossRef]

11.   Zhang, X.; Shi, F.; Niu, J.; Jiang, Y.G.; Wang, Z.Q. Superhydrophobic surfaces: From structural control to functional application. *J. Mater. Chem.* **2008**, *18*, 621–633. [CrossRef]

12.   Sun, T.L.; Feng, L.; Gao, X.F.; Jiang, L. Bioinspired Surfaces with Special wettability. *Acc. Chem. Res.* **2005**, *38*, 644–652. [CrossRef] [PubMed]

13.   Callies, M.; Quere, D. On water repellency. *Soft Matter* **2005**, *1*, 55–61. [CrossRef]

14.   Shirtcliffe, N.J.; McHale, G.; Newton, M.I. The superhydrophobicity of polymer surfaces: Recent developments. *J. Polym. Sci. Part. B Polym. Phys.* **2011**, *49*, 1203–1217. [CrossRef]

15.   Arkles, B.; Pan, Y.; Kim, Y.M. The Role of Polarity in the Structure of Silanes Employed in Surface Modification. In *Silanes and Other Coupling Agents*; Mittal, K.I., Ed.; VSP: Leiden, The Netherlands, 2009; pp. 51–65.

16.   Parale, V.G.; Mahadik, D.B.; Mahadik, S.A. OTES modified transparent dip coated silica coatings. *Ceram. Int.* **2013**, *39*, 835–840. [CrossRef]

17.   Bouvet-Marchand, A.; Graillot, A.; Abel, M.; Koudia, M.; Boutevin, G.; Loubat, C.; Grosso, D. Distribution of fluoroalkylsilanes in hydrophobic hybrid sol–gel coatings obtained by co-condensation. *J. Mater. Chem. A* **2018**, *6*, 24899–24910. [CrossRef]

18.   Gautam, K.S.; Dhinojwala, A. Molecular Structure of Hydrophobic Al kyl Side Chains at Comb Polymer-Air Interface. *Macromolecules* **2001**, *34*, 1137–1139. [CrossRef]

19.   Pagliaro, M.; Ciriminna, R.J. New fluorinated functional materials. *Mater. Chem.* **2005**, *15*, 4981–4991. [CrossRef]

20.   Brendel, S.; Fetter, E.; Staude, C.; Vierke, L.; Biegel-Engler, A. Short-chain perfluoroalkyl acids: Environmental concerns and a regulatory strategy under REACH. *Environ. Sci. Eur.* **2018**, *30*, 9–20. [CrossRef]

21.   Available online: https://echa.europa.eu/de/-/five-european-states-call-for-evidence-on-broad-pfas-restriction (accessed on 20 May 2020).

22.   Nguyen-Tri, P.; Tran, H.N.; Plamondon, C.O.; Tuduri, L.; Vo, D.-V.N.; Nanda, S.; Mishra, A.; Chao, H.-P.; Bajpai, A.K. Recent progress in the preparation, properties and applications of superhydrophobic nano-based coatings and surfaces: A review. *Prog. Org. Coat.* **2019**, *132*, 235–256. [CrossRef]

23.   Nguyen-Tri, P.; Nguyen, T.A.; Carriere, P.; Ngo Xuan, C. Nanocomposite coatings: Preparation, characterization, properties, and applications. *Int. J. Corros.* **2018**, *2018*, 4749501. [CrossRef]

24.   Brink, G.H.; Foley, N.; Zwaan, D.; Kooi, B.J.; Palasantzas, G. Roughness controlled superhydrophobicity on single nanometer length scale with metal nanoparticles. *RSC Adv.* **2015**, *5*, 28696–28702. [CrossRef]

25.   Milionis, A.; Martiradonna, L.; Anyfantis, G.C.; Cozzoli, P.D.; Bayer, I.S.; Fragouli, D.; Athanassiou, A. Control of the water adhesion on hydrophobic micropillars by spray coating technique. *Colloid Polym. Sci.* **2013**, *291*, 401–407. [CrossRef]

26.   Gao, N.; Yan, Y. Characterisation of surface wettability based on nanoparticles. *Nanoscale* **2012**, *4*, 2202–2218. [CrossRef]

27.   Wu, Y.; Li, X.; Mi, C.; Zong, L.; Wang, X. Preparation and characterization of perfluorine-SiO2 nanoparticles and superhydrophobic fluorosilicone/silica hybrid composite coating. *Appl. Phys. A* **2019**, *125*, 250–263. [CrossRef]

28. Zhou, H.; Yea, Q.; Xu, J. Polyhedral oligomeric silsesquioxane-based hybrid materials and their applications. *Mater. Chem. Front.* **2017**, *1*, 212–230. [CrossRef]

29. Ayandele, E.; Sarkar, B.; Alexandridis, P. Polyhedral Oligomeric Silsesquioxane (POSS)-Containing Polymer Nanocomposites. *Nanomaterial* **2012**, *2*, 445–475. [CrossRef] [PubMed]

30. Raftopoulos, K.N.; Pielichowski, K. Segmental dynamics in hybrid polymer/POSS nanomaterials. *Prog. Polym. Sci.* **2016**, *52*, 136–187. [CrossRef]

31. Kuo, S.W. Building Blocks Precisely from Polyhedral Oligomeric Silsesquioxane Nanoparticles. *ACS Cent. Sci.* **2016**, *2*, 62–64. [CrossRef] [PubMed]

32. D'Arienzo, M.; Diré, S.; Redaelli, M.; Borovin, E.; Callone, E.; Di Credico, B.; Morazzoni, F.; Pegoretti, A.; Scotti, R.J. Unveiling the hybrid interface in polymer nanocomposites enclosing silsesquioxanes with tunable molecular structure: Spectroscopic, thermal and mechanical properties. *Colloid Interface Sci.* **2018**, *512*, 609–617. [CrossRef]

33. Kuo, S.W.; Chang, F.C. POSS related polymer nanocomposites. *Prog. Polym. Sci.* **2011**, *36*, 1649–1696. [CrossRef]

34. Fina, A.; Monticelli, O.; Camino, G.J. POSS-based hybrids by melt/reactive blending. *Mater. Chem.* **2010**, *20*, 9297–9305. [CrossRef]

35. Tanaka, K.; Chujo, Y.J. Advanced functional materials based on polyhedral oligomeric silsesquioxane (POSS). *Mater. Chem.* **2012**, *22*, 1733–1750. [CrossRef]

36. D'Arienzo, M.; Redaelli, M.; Callone, E.; Conzatti, L.; Di Credico, B.; Dirè, S.; Giannini, L.; Polizzi, S.; Schizzi, I.; Scotti, R.; et al. Hybrid SiO2@POSS nanofiller: A promising reinforcing system for rubber nanocomposites. *Mater. Chem. Front.* **2017**, *1*, 212–230. [CrossRef]

37. Redaelli, M.; D'Arienzo, M.; Brus, J.; Di Credico, B.; Geppi, M.; Giannini, L.; Matejka, L.; Martini, F.; Panattoni, F.; Spirkova, M.; et al. On the key role of SiO2@POSS hybrid filler in tailoring networking and interfaces in rubber nanocomposites. *Polym. Test.* **2018**, *65*, 429–439. [CrossRef]

38. Cordes, D.B.; Lickiss, P.D.; Rataboul, F. Recent Developments in the Chemistry of Cubic Polyhedral Oligosilsesquioxanes. *Chem. Rev.* **2010**, *110*, 2081–2173. [CrossRef]

39. Dirè, S.; Borovin, E.; Ribot, F. Architecture of Silsesquioxanes. In *Handbook of Sol-Gel Science and Technology*; Klein, L., Aparicio, M., Jitianu, A., Eds.; Springer: New York, NY, USA, 2016; pp. 1–34.

40. Choi, S.; Lee, A.S.; Hwang, S.S.; Baek, K. Structural Control of Fully Condensed Polysilsesquioxanes: Ladderlike vs Cage Structured Polyphenylsilsesquioxanes. *Macromolecules* **2015**, *48*, 6063–6070. [CrossRef]

41. Huoa, L.; Dub, P.; Zhoua, H.; Zhanga, K.; Liu, P. Fabrication and tribological properties of self-assembled monolayer of n-alkyltrimethoxysilane on silicon: Effect of SAM alkyl chain length. *Appl. Surf. Sci.* **2017**, *396*, 865–869. [CrossRef]

42. Mabry, J.M.; Vij, A.; Iacono, S.T. Fluorinated Polyhedral Oligomeric Silsesquioxanes (F-POSS). *Angew. Chem.* **2008**, *120*, 4205–4208. [CrossRef]

43. Liu, M.; Zhang, X.; Wang, D.; Cheng, J.; Pang, X.; Qu, W.; Li, C.; Li, S. Facile Fabrication of Superhydrophobic Surface from Fluorinated POSS Acrylate Copolymer via One-Step Breath Figure Method and Its Anti-Corrosion Property. *Polymers* **2019**, *11*, 1953. [CrossRef]

44. Kim, K.; Lichtenhan, J.D.; Otaigbe, J.U. Facile route to nature inspired hydrophobic surface modification of phosphate glass using polyhedral oligomeric silsesquioxane with improved properties. *Appl. Surf. Sci.* **2019**, *470*, 733–743. [CrossRef]

45. Marcinkowska, A.; Przadka, D.; Andrzejewska, E.J. POSS functionalized with mixed fluoroalkyl and methacryloxy substituents as modifiers for UV-curable coatings. *Coat. Technol. Res.* **2019**, *16*, 167–178. [CrossRef]

46. Meuler, A.J.; Chhatre, S.S.; Nieves, A.R.; Mabry, J.M.; Cohen, R.E.; McKinley, G.H. Examination of wettability and surface energy in fluorodecyl POSS/polymer blends. *Soft Matter* **2011**, *7*, 10122–10134. [CrossRef]

47. Dodiuk, H.; Rios, P.F.; Dotan, A.; Kenig, S. Hydrophobic and self-cleaning coatings. *Polym. Adv. Technol.* **2007**, *18*, 746–750. [CrossRef]

48. Foorginezhad, S.; Zerafat, M.M. Fabrication of superhydrophobic coatings with self-cleaning properties on cotton fabric based on Octa vinyl polyhedral oligomeric silsesquioxane/polydimethylsiloxane (OV-POSS/PDMS) nanocomposite. *J. Colloid Interface Sci.* **2019**, *540*, 78–87. [CrossRef] [PubMed]

49. Yamamoto, K.; Kawaguchi, D.; Abe, T.; Komino, T.; Mamada, M.; Kabe, T.; Adachi, C.; Naka, K.; Tanaka, K. Surface Segregation of a Star-Shaped Polyhedral Oligomeric Silsesquioxane in a Polymer Matrix. *Langmuir* **2020**, *36*, 9960–9966. [CrossRef]

50. Choi, S.S.; Lee, A.S.; Lee, H.S.; Jeon, H.Y.; Baek, K.Y.; Choi, D.H.; Hwang, S.S. Synthesis and characterization of UV-curable ladder-like polysilsesquioxane. *J. Polym. Sci. Part. A Polym. Chem.* **2011**, *49*, 5012–5018. [CrossRef]

51. Lee, A.S.S.; Choi, S.S.; Lee, H.S.; Jeon, H.Y.; Baek, K.Y.; Hwang, S.S. Synthesis and characterization of organic–inorganic hybrid block copolymers containing a fully condensed ladder-like polyphenylsilsesquioxane. *J. Polym. Sci. Part A Polym. Chem.* **2012**, *50*, 4563–4570. [CrossRef]

52. Lee, A.S.; Lee, J.H.; Lee, J.; Hong, S.M.; Hwang, S.M.; Min Koo, C.J. Novel polysilsesquioxane hybrid polymer electrolytes for lithium ion batteries. *Mater. Chem. A* **2014**, *2*, 1277–1283.

53. Zhang, Z.X.; Hao, J.; Xie, P.; Zhang, X.; Han, C.C.; Zhang, R. A Well-Defined Ladder Polyphenylsilsesquioxane (Ph-LPSQ) Synthesized via a New Three-Step Approach: Monomer Self-Organization–Lyophilization—Surface-Confined Polycondensation. *Chem. Mater.* **2008**, *20*, 1322–1330. [CrossRef]

54. Prado, L.A.S.D.A.; Radovanovic, E.; Pastore, H.O.; Yoshida, I.V.P.; Torriani, I.L. Poly(phenylsilsesquioxane)s: Structural and morphological characterization. *J. Polym. Sci. Part. A Polym. Chem.* **2000**, *38*, 1580–1589. [CrossRef]

55. Kim, Y.H.; Choi, G.M.; Bae, J.G.; Kim, Y.H. High-Performance and Simply-Synthesized Ladder-Like Structured Methacrylate Siloxane Hybrid Material for Flexible Hard Coating. *Polymers* **2018**, *10*, 449. [CrossRef] [PubMed]

56. Lee, A.S.; Jo, Y.Y.; Jeon, H.; Choi, S.-S.; Baek, K.-Y.; Hwang, S.S. Mechanical properties of thiol-ene UV-curable thermoplastic polysilsesquioxanes. *Polymer* **2015**, *68*, 140–146. [CrossRef]

57. Park, S.; Lee, A.S.; Do, Y.S.; Kim, J.F.; Hwang, S.S.; Lee, Y.M.; Lee, J.H.; Lee, J.S. Side-chain engineering of ladder-structured polysilsesquioxane membranes for gas separations. *J. Membr. Sci.* **2016**, *516*, 202–214. [CrossRef]

58. Zhang, C.; Zhang, C.; Ding, R.; Cui, X.; Wang, J.; Zhang, Q.; Xu, Y. New Water Vapor Barrier Film Based on Lamellar Aliphatic-Monoamine-Bridged Polysilsesquioxane. *ACS Appl. Mater. Interfaces* **2016**, *8*, 14766–14775. [CrossRef] [PubMed]

59. Jo, C.I.; Ko, J.U.; Yin, Z.X.; Kim, Y.J.; Kim, Y.S. Solvent-Free and Highly Transparent SiO2 Nanoparticle–Polymer Composite with an Enhanced Moisture Barrier Property. *Ind. Eng. Chem. Res.* **2016**, *55*, 9433–9439. [CrossRef]

60. Kopanati, G.N.; Seethamraju, S.; Ramamurthy, P.C.; Madras, G. A Surlyn/magnesium oxide nanocomposite as an effective water vapor barrier for organic device encapsulation. *RSC Adv.* **2015**, *5*, 32580–32587. [CrossRef]

61. Saravanan, S.; Gupta, S.; Ramamurthy, P.C.; Madras, G. Effect of silane functionalized alumina on poly(vinyl butyral) nanocomposite films: Thermal, mechanical, and moisture barrier studies. *Polym. Compos.* **2014**, *35*, 1426–1435. [CrossRef]

62. Scotti, R.; Conzatti, L.; D'Arienzo, M.; Di Credico, B.; Giannini, L.; Hanel, T.; Stagnaro, P.; Susanna, A.; Tadiello, L.; Morazzoni, F. Shape controlled spherical (0D) and rod-like (1D) silica nanoparticles in silica/styrene butadiene rubber nanocomposites: Role of the particle morphology on the filler reinforcing effect. *Polymer* **2014**, *55*, 1497–1506. [CrossRef]

63. Gao, L.; McCarthy, T.J. Teflon is Hydrophilic. Comments on Definitions of Hydrophobic, Shear versus Tensile Hydrophobicity, and Wettability Characterization. *Langmuir* **2008**, *24*, 9183–9188. [CrossRef]

64. McHale, G. All Solids, Including Teflon, Are Hydrophilic (To Some Extent), But Some Have Roughness Induced Hydrophobic Tendencies. *Langmuir* **2009**, *25*, 7185–7187. [CrossRef]

65. Lee, J.B.; Dos Santos, S.; Antonini, C. Water Touch-and-Bounce from a Soft Viscoelastic Substrate: Wetting, Dewetting, and Rebound on Bitumen. *Langmuir* **2016**, *32*, 8245–8254. [CrossRef] [PubMed]

66. Borovin, E.; Callone, E.; Ceccato, R.; Quaranta, A.; Dirè, S. Adsorptive properties of sol–gel derived hybrid organic/inorganic coatings. *Mater. Chem. Phys.* **2014**, *147*, 954–962. [CrossRef]

67. D'Arienzo, M.; Diré, S.; Masneri, V.; Rovera, D.; Di Credico, B.; Callone, E.; Mascotto, S.; Pegoretti, A.; Ziarelli, F.; Scotti, R. Tailoring the Dielectric and Mechanical Properties of Polybutadiene Nanocomposites by Using Designed Ladder-like Polysilsesquioxanes. *ACS Appl. Nano Mater.* **2018**, *1*, 3817–3828. [CrossRef]

68. Di Maggio, R.; Callone, E.; Girardi, F.; Diré, S.J. Structure-related behavior of hybrid organic–inorganic materials prepared in different synthesis conditions from Zr-based NBBs and 3-methacryloxypropyl trimethoxysilane. *Appl. Polym. Sci.* **2012**, *125*, 1713–1723. [CrossRef]

69. Seki, H.; Kajiwara, T.; Abe, Y.; Gunji, T.J. Synthesis and structure of ladder polymethylsilsesquioxanes from sila-functionalized cyclotetrasiloxanes. *Organomet. Chem.* **2010**, *695*, 1363–1369. [CrossRef]

70. Nimmo, J.P.; Kroll, P.J. First-Principles Calculations and Analysis of 29Si Nuclear Magnetic Resonance Chemical Shifts in Silicon Oxycarbide Ceramics. *Phys. Chem. C* **2014**, *118*, 29952–29961. [CrossRef]

71. Kang, W.; An, G.; Kim, M.J.; Lee, W.H.; Lee, D.Y.; Kim, H.; Cho, J.H. Ladder-Type Silsesquioxane Copolymer Gate Dielectrics for High-Performance Organic Transistors and Inverters. *J. Phys. Chem. C* **2016**, *120*, 3501–3508. [CrossRef]

72. Kim, M.J.; Heo, Y.M.; Cho, J.H. Ladder-type silsesquioxane copolymer gate dielectrics for gating solution-processed IGZO field-effect transistors. *Org. Electron.* **2017**, *43*, 41–46. [CrossRef]

73. Turri, S.; Levi, M. Wettability of Polyhedral Oligomeric Silsesquioxane Nanostructured Polymer Surfaces. *Macromol. Rapid Commun.* **2005**, *26*, 1233–1236. [CrossRef]

74. Neumann, A.W.; Good, R.J. Thermodynamics of contact angles. I. Heterogeneous solid surfaces. *J. Colloid Interface Sci.* **1972**, *38*, 341–358. [CrossRef]

75. Schulze, R.D.; Possart, W.; Kamusewitz, H.; Bischof, C.J. Young's equilibrium contact angle on rough solid surfaces. Part I. An empirical determination. *Adhes. Sci. Technol.* **1989**, *3*, 39–48. [CrossRef]